NUMERICAL SIMULATION OF TURBULENT FLOW AND FIRE PROPAGATION IN COMPLEX TOPOGRAPHY

A. M. G. Lopes
Grupo de Mecânica dos Fluidos, Universidade de Coimbra,
3000 Coimbra, Portugal

A. C. M. Sousa
Department of Mechanical Engineering, University of New Brunswick,
Fredericton, New Brunswick, E3B 5A3 Canada

D. X. Viegas
Grupo de Mecânica dos Fluidos, Universidade de Coimbra,
3000 Coimbra, Portugal

A numerical model is presented for the simultaneous calculation of velocity and temperature fields, and fire propagation in mountain ridges. Turbulent fluid flow calculations are performed using the SIMPLEC *procedure applied to a boundary-fitted coordinate system, while the fire rate of spread is computed using a combination of Rothermel's fire spread model, a two-semi-ellipse formulation for fire shape, and the Dijkstra dynamic programming algorithm for fire growth simulation. To assess the influence of the ridge geometry upon isothermal flow, calculations are carried out for different height configurations. Fire computations are then made for the same configurations, and for each configuration, two types of fuel are tested. Results show a higher rate of spread for the ridge with the lower intersection angle, confirming observations that report unusually high propagation rates of fires in these topographies.*

INTRODUCTION

Wildland fires occurring in complex terrain very often take on dramatic proportions, which may result in high material costs, not to mention tragic loss of human lives. Among large fires that occur worldwide, a few have been singled out due to dangerous behavior. The aim of the present paper is to provide a better understanding of the high propagation rates of fires occurring in mountain ridges, a topography that, in the past, has been related to large, lethal fires. This topography can be visualized as the intersection of two inclined slopes with the

NOMENCLATURE

$a_E, a_W, \ldots$	coefficients of the discretized equations	u_p	velocity component parallel to the wall
a_1, a_2	variables in the ellipse definition	U, V, W	contravariant velocity components
A	burned and burning areas	U_i	$U_1 = U, U_2 = V, U_3 = W$
c, p, b, d	variables in the ellipse definition	U_0	free stream velocity; incident wind speed
c_p	pressure coefficient	V_{eq}	equivalent wind speed
C_1, C_2, C_3	turbulence model constants	V_s	wind speed equivalent to slope
D_1, E	turbulence model constants	V_w	wind speed at midflame height
f_1, f_μ	damping functions in the turbulence model	Vel	local velocity magnitude
g^{ij}	contravariant metric relations	x, y, z	axis of Cartesian coordinate system
g_i	gravity acceleration in direction i	x_i	$x_1 = x, x_2 = y, x_3 = z$
G	buoyancy term in the turbulence model	α, θ, ψ	angles characterizing the ridge
I_r	reaction intensity	Γ	generic diffusion coefficient
J	Jacobian of the transformation	δ_{ij}	Kronecker delta
k	turbulence kinetic energy	$\varepsilon, \tilde{\varepsilon}$	total and isotropic dissipation of turbulent kinetic energy
n	distance to the wall		
P	pressure	μ, μ_t	dynamic viscosity (laminar and turbulent)
P'	pressure correction		
P_f, Q_f, R_f	control functions	μ_{eff}	effective dynamic viscosity $(= \mu + \mu_t)$
P_s	reference pressure		
P_w	wall static pressure	ξ, η, ζ	axis of the curvilinear coordinate system
P_1	production of turbulent kinetic energy	ξ_i	$\xi_1 = \xi, \xi_2 = \eta, \xi_3 = \zeta$
Q_i	heat of pre-ignition	π	propagating flux ratio
$\mathbf{R}$	rate of spread	ρ	density
Re_{kn}	local turbulence Reynolds number	ρ_b	bulk density
Re_t	turbulence Reynolds number	ρ_0	reference density
S_c, S_ϕ	generic source term	σ_1	laminar Prandtl number
S^*, S^{**}	source terms in P' equation	$\sigma_t, \sigma_k, \sigma_\varepsilon$	turbulent Prandtl number for T, k, and ε
t	time		
T	temperature	ϕ	generic variable
u, v, w	Cartesian velocity components	ϕ_f, ψ_f	control functions
u^*, v^*, w^*	starred velocities	$\mathbf{\phi}_s, \mathbf{\phi}_w$	slope and wind factors
u_i	$u_1 = u, u_2 = v, u_3 = w$	ω	effective heating number

ground, as shown in Figure 1. It is widely recognized that the ability to predict the rate of spread of a fire is of outmost importance for planning an efficient attack and rapid suppression. Among the several models that have been proposed to describe the rate of spread of wind-driven fires, Rothermel's model [1], with its application in the Behave system [2], has been one of the most popular and widely used fire-spread models. This system, however, requires a priori knowledge of the midflame wind speed, which limits its use for complex terrain topography, where wind speed is extremely difficult to estimate. The present approach is designed to bridge this gap, by proposing a computational procedure that integrates a numerical algorithm for turbulent three-dimensional flow calculations over general topography with a fire propagation model based on Rothermel's work for the calculation of fire spread.
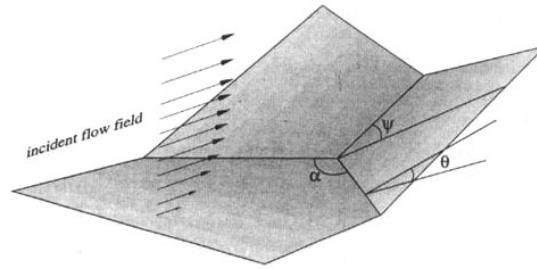
Figure 1. Ridge geometrical parameters.

GRID GENERATION

For appropriate discretization of the equations in the selected domain, a boundary-fitted coordinate system is employed, by which a complex physical region is transformed into a "regular" computational domain. The use of a generalized coordinate system allows the integration of the transport equations governing fluid motion to be done in the computational domain (ξ, η, ζ), which for convenience, may be taken as cubic with a unit mesh spacing. This procedure greatly simplifies the numerical procedure, since the resolution of the transport equations is carried out in a rectangular region, where their integration, as well as the imposition of boundary conditions, is more straightforward and accurate than if a Cartesian system was employed.

The accuracy of the solution obtained and its numerical stability are highly dependent on the grid used, which should be smooth, refined in locations where high gradients are expected to occur, and with a low degree of skewness. To meet these requirements, in the present work a nonorthogonal three-dimensional grid was generated by solving a set of elliptic equations, the mathematical formulation of which is presented in Eq. (1), and which expresses a relation between the physical (x, y, z) and computational (ξ, η, ζ) coordinates.

$$\xi_{xx} + \xi_{yy} + \xi_{zz} = P_f(\xi, \eta, \zeta) + \phi_f(\xi, \eta, \zeta)|\Delta\xi|^2$$

$$\eta_{xx} + \eta_{yy} + \eta_{zz} = Q_f(\xi, \eta, \zeta) + \psi_f(\xi, \eta, \zeta)|\Delta\eta|^2 \qquad (1)$$

$$\zeta_{xx} + \zeta_{yy} + \zeta_{zz} = R_f(\xi, \eta, \zeta)$$

This method was developed by Thompson et al. [3], and further refined by other authors through the introduction of specific control functions. These control functions are designed to allow proper adjustment of the clustering (control function R_f) and orthogonality (control functions P_f and Q_f) of grid lines near the boundaries. Provisions may also be made to transmit the grid spacing to the interior of the domain (control functions ϕ_f and Ψ_f). Since the above equations are to be solved in the computational domain, the dependent and independent variables must be interchanged, yielding the following system of equations:

$$\alpha_1(r_{\xi\xi} + \phi_f r_\xi) + \alpha_2(r_{\eta\eta} + \Psi_f r_\eta) + \alpha_3(r_{\xi\xi}) + 2(\beta_1 r_{\xi\eta} + \beta_2 r_{\eta\zeta} + \beta_3 r_{\zeta\xi})$$

$$= -J^2(P_f r_\xi + Q_f r_\eta + R_f r_\zeta)$$

$$\alpha_1 = J^2(\nabla\xi \cdot \nabla\xi) \quad \alpha_2 = J^2(\nabla\eta \cdot \nabla\eta) \quad \alpha_3 = J^3(\nabla\zeta \cdot \nabla\zeta) \tag{2}$$

$$\beta_1 = J^2(\nabla\xi \cdot \nabla\eta) \quad \beta_2 = J^2(\nabla\eta \cdot \nabla\zeta) \quad \beta_3 = J^2(\nabla\zeta \cdot \nabla\xi)$$

where $r = (x, y, z)$.

These equations are discretized in the computational domain using second-order differencing and are solved with an iterative numerical technique. The boundary conditions for these equations are imposed by specifying the physical coordinates of the boundary grid points defined on two opposite boundaries.

NUMERICAL METHOD FOR FLUID FLOW AND TEMPERATURE CALCULATIONS

Transport Equations

The wind field required as an input for the fire propagation model is obtained through the solution of the steady-state Navier-Stokes (NS) equations formulated in a boundary fitted coordinate system. The Boussinesq approximation for the density variations is not employed, and the governing equations written in their tensorial Cartesian form are:

Conservation of momentum

$$\frac{\partial}{\partial x_j}(\rho u_i u_j) = -\frac{\partial P}{\partial x_i} + \frac{\partial}{\partial x_i}\left[\Gamma\left(2\frac{\partial u_i}{\partial x_i} - \frac{2}{3}\text{div }\mathbf{V}\right)\right]$$

$$+ \frac{\partial}{\partial x_j}\left[\Gamma\left(\frac{\partial u_i}{\partial x_j} + \frac{\partial u_j}{\partial x_i}\right)\right] - \frac{2}{3}\frac{\partial(\rho k)}{\partial x_i} + \rho g_i \tag{3a}$$

where $\Gamma = \mu + \mu_t$.
Conservation of mass

$$\frac{\partial(\rho u_i)}{\partial x_i} = 0 \tag{3b}$$

Conservation of energy

$$\frac{\partial}{\partial x_i}(\rho u_i T) = \frac{\partial}{\partial x_i}\left(\Gamma\frac{\partial T}{\partial x_i}\right) + \frac{S_T}{c_p} \tag{3c}$$

where $\Gamma = (\mu/\sigma_1) + (\mu_t/\sigma_t)$.

Turbulence effects upon the mean flow and temperature fields are modeled through the eddy viscosity concept, which states that turbulent stresses are related to the mean strain rate via the turbulent viscosity by the following equation:

$$-\rho\overline{u_i' u_j'} = \mu_t\left(\frac{\partial u_i}{\partial x_j} + \frac{\partial u_j}{\partial x_i}\right) - \frac{2}{3}\delta_{ij}\left(\mu_t\frac{\partial u_k}{\partial x_k} + \rho k\right) \tag{4}$$

The calculation of the eddy viscosity is performed with a low Reynolds number k-ε model, in a formulation similar to the one proposed by Zhang and Sousa [4], but extended to generalized coordinates in three dimensions. The

Cartesian form of the corresponding equations is

$$\frac{\partial}{\partial x_i}(\rho u_i k) = \frac{\partial}{\partial x_i}\left[\left(\mu + \frac{\mu_t}{\sigma_k}\right)\frac{\partial k}{\partial x_i}\right] + P_1 + G - \rho\tilde{\varepsilon} + D_1$$

where

$$P_1 = -\overline{\rho u'_i u'_j}\frac{\partial u_i}{\partial x_j} \tag{5}$$

$$\tilde{\varepsilon} = \varepsilon + D_1 \qquad \mu_t = f_\mu\frac{C_\mu \rho k^2}{\tilde{\varepsilon}} \qquad G = -\beta g\frac{\mu_t}{\sigma_t}\frac{\partial T}{\partial z}$$

$$D_1 = -2\mu\left(\frac{\partial\sqrt{k}}{\partial n}\right)^2 \qquad \mathrm{Re}_t = \frac{\rho k^2}{\mu\tilde{\varepsilon}}$$

$$\frac{\partial}{\partial x_i}(\rho u_i\tilde{\varepsilon}) = \frac{\partial}{\partial x_i}\left(\frac{\partial\tilde{\varepsilon}}{\partial x_i}\right) + \frac{\tilde{\varepsilon}}{k}[C_1(P_1 + C_3 G) - C_2 f_1 \rho\tilde{\varepsilon}] + E$$

$$f_\mu = \left[1 - \exp\left(-\frac{\mathrm{Re}_{kn}}{26.5}\right)\right]^2$$

$$f_1 = 1 - 0.3\exp(-\mathrm{Re}_t^2) \qquad E = \frac{\mu\mu_t(1 - f_\mu)^2}{\rho}$$

$$\mathrm{Re}_{kn} = \frac{\rho\sqrt{k}\,n}{\mu}$$

$$C_\mu = 0.09 \qquad C_1 = 1.45 \qquad C_2 = 1.9$$

$$C_3 = \tanh\left|\frac{w}{u}\right| \qquad \sigma_k = 1 \qquad \sigma_\varepsilon = 1.3$$

The variables n and u_p, in the original formulation [4], were taken as the normal distance to the closest wall and the velocity component parallel to the wall, respectively.

Transformation of the Equations

The original transport equations presented above are transformed from the physical domain (x, y, z) to the computational domain (ξ, η, ζ) through the substitution of the independent Cartesian variables by the deformed grid variables. In the present approach, the Cartesian components of the velocity are kept as the dependent variables, since the choice of the covariant or the contravariant velocity components would lead to a much more complicated set of equations. Thus, a partial transformation is used, as opposed to a total transformation, which is

accomplished by application of the chain rule:

$$\frac{\partial \phi}{\partial x_i} = \frac{\partial \xi}{\partial x_i}\frac{\partial \phi}{\partial \xi} + \frac{\partial \eta}{\partial x_i}\frac{\partial \phi}{\partial \eta} + \frac{\partial \zeta}{\partial x_i}\frac{\partial \phi}{\partial \zeta}$$

$$= \xi_{x_i}\frac{\partial \phi}{\partial \xi} + \eta_{x_i}\frac{\partial \phi}{\partial \eta} + \zeta_{x_i}\frac{\partial \phi}{\partial \zeta} \tag{6}$$

where ξ_{x_i} are the metrics of the transformation. After Eq. (6) is used for substitution of the dependent variables, the metric identity, the mathematical formulation of which is given by

$$\frac{\partial}{\partial \xi}(J\xi_{x_i}) + \frac{\partial}{\partial \eta}(J\eta_{x_i}) + \frac{\partial}{\partial \zeta}(J\zeta_{x_i}) = 0 \tag{7}$$

is evoked to set the transformed equations in the strong conservation law form [5].

The resulting set of equations, written in terms of a generic velocity component u_i, is as follows:

Momentum equations

$$\frac{\partial}{\partial \xi_j}(J\rho U_j u_i) = -\frac{\partial \xi_j}{\partial x_i}\frac{\partial P}{\partial \xi_j} + \frac{\partial}{\partial \xi_m}\mu_{\text{eff}}J$$

$$\cdot\left(g^{mn}\frac{\partial u_i}{\partial \xi_n} + \frac{\partial \xi_m}{\partial x_j}\frac{\partial \xi_n}{\partial x_i}\frac{\partial u_j}{\partial \xi_n} - \frac{2}{3}\frac{\partial \xi_m}{\partial x_i}\frac{\partial \xi_n}{\partial x_j}\frac{\partial u_j}{\partial \xi_n}\right)$$

$$-\frac{2}{3}J\left(\frac{\partial \xi_j}{\partial x_i}\frac{\partial(\rho k)}{\partial \xi_j}\right) - Jg_i(\rho - \rho_0) \tag{8}$$

Continuity equation

$$\frac{\partial}{\partial \xi_i}(\rho J U_i) = 0 \tag{9}$$

For a generic scalar ϕ, which in the present work stands for T, k, or $\tilde{\varepsilon}$, the corresponding transport equation in the computational domain is

$$\frac{\partial}{\partial \xi_i}(J\rho U_i \phi) = \frac{\partial}{\partial \xi_i}\left[J\Gamma\left(g^{ij}\frac{\partial \phi}{\partial \xi_j}\right)\right] + JS_\phi \tag{10}$$

where S_ϕ is a general source term. In the previous equations, U_i represent the contravariant components of the velocity vector, defined as

$$U_1 = U = \xi_x u + \xi_y v + \xi_z w \qquad U_2 = V = \eta_x u + \eta_y v + \eta_z w$$

$$U_3 = W = \zeta_x u + \zeta_y v + \zeta_z w \tag{11}$$

where J is the transformation Jacobian:

$$J = \begin{vmatrix} x_\xi & x_\eta & x_\zeta \\ y_\xi & y_\eta & y_\zeta \\ z_\xi & z_\eta & z_\zeta \end{vmatrix} \tag{12}$$

The contravariant metric relations g^{ij},

$$g^{ij} = \frac{\partial \xi_i}{\partial x_m} \frac{\partial \xi_j}{\partial x_m} \tag{13}$$

are computed numerically through the contravariant metric relations [5], applying central differences to the coordinates of the grid points represented by triangles in Figure 2.

Numerical Algorithm

A staggered grid [6] is adopted for the location of the three components of the velocity vector, which are located at the center of each face of the control volume (contravariant positions). Other scalars, such as temperature and turbulence quantities, are positioned at the geometric center of the control volumes, as shown in Figure 2. A control volume approach is employed for the integration of the transport equations in each computational cell [7], which for convenience, is cubic with a unit mesh spacing. The integration is performed using piecewise linear profiles for the viscous derivatives, while the convection terms are treated using a hybrid formulation [7]. The discretized equations are then cast in the following single general form:

$$a_P \phi_P = \Sigma a_{nb} \phi_{nb} + S_\phi \qquad \Sigma a_{nb} \phi_{nb} = a_E \phi_E + a_W \phi_W + a_N \phi_N + a_S \phi_S$$
$$+ a_T \phi_T + a_B \phi_B \tag{14}$$

where E is east, W is west, N is north, S is south, T is top, B is bottom, ϕ is a generic variable, and S_ϕ is the source term.

Continuity and momentum equations are linked through pressure following the SIMPLEC procedure [8], in a formulation adapted to a boundary-fitted coordi-
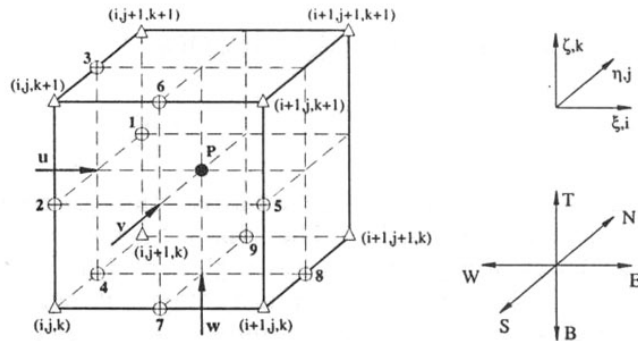

Figure 2. Typical control volume in the computational domain.

nate system. For this purpose, three simplified momentum equations are written in each contravariant position of the control volume. Substitution of these equations in the continuity equation allows the obtainment of the following pressure correction equation:

$$A_{\mathrm{P}} P'_{\mathrm{P}} = \sum A_{\mathrm{nb}} P'_{\mathrm{nb}} + S^* + S^{**} \tag{15}$$

where

$$
\begin{aligned}
S^{**} = {} & \left[\frac{\rho J^2}{a_{\mathrm{P}}^u - \sum a_{\mathrm{nb}}} \left(g^{12} \frac{\partial P'}{\partial \eta} + g^{13} \frac{\partial P'}{\partial \zeta} \right) \right]_{\mathrm{E}} \\
& - \left[\frac{\rho J^2}{a_{\mathrm{P}}^u - \sum a_{\mathrm{nb}}} \left(g^{12} \frac{\partial P'}{\partial \eta} + g^{13} \frac{\partial P'}{\partial \zeta} \right) \right]_{\mathrm{W}} \\
& + \left[\frac{\rho J^2}{a_{\mathrm{P}}^v - \sum a_{\mathrm{nb}}} \left(g^{21} \frac{\partial P'}{\partial \xi} + g^{23} \frac{\partial P'}{\partial \zeta} \right) \right]_{\mathrm{N}} \\
& - \left[\frac{\rho J^2}{a_{\mathrm{P}}^v - \sum a_{\mathrm{nb}}} \left(g^{21} \frac{\partial P'}{\partial \xi} + g^{23} \frac{\partial P'}{\partial \zeta} \right) \right]_{\mathrm{S}} \\
& + \left[\frac{\rho J^2}{a_{\mathrm{P}}^w - \sum a_{\mathrm{nb}}} \left(g^{31} \frac{\partial P'}{\partial \xi} + g^{32} \frac{\partial P'}{\partial \eta} \right) \right]_{\mathrm{T}} \\
& - \left[\frac{\rho J^2}{a_{\mathrm{P}}^w - \sum a_{\mathrm{nb}}} \left(g^{31} \frac{\partial P'}{\partial \xi} + g^{32} \frac{\partial P'}{\partial \eta} \right) \right]_{\mathrm{B}}
\end{aligned}
$$

and

$$
\begin{aligned}
S^* = {} & \left[(\rho J)(\xi_x u^* + \xi_y v^* + \xi_z w^*) \right]_{\mathrm{E}} - \left[(\rho J)(\xi_x u^* + \xi_y v^* + \xi_z w^*) \right]_{\mathrm{W}} \\
& + \left[(\rho J)(\eta_x u^* + \eta_y v^* + \eta_z w^*) \right]_{\mathrm{N}} - \left[(\rho J)(\eta_x u^* + \eta_y v^* + \eta_z w^*) \right]_{\mathrm{S}} \\
& + \left[(\rho J)(\zeta_x u^* + \zeta_y v^* + \zeta_z w^*) \right]_{\mathrm{T}} - \left[(\rho J)(\zeta_x u^* + \zeta_y v^* + \zeta_z w^*) \right]_{\mathrm{B}}
\end{aligned}
$$

In the equations above, u^*, v^*, and w^* are the starred velocities, obtained through the solution of the momentum equations. The term S^{**} is quite small in comparison with the other terms of Eq. (15) and was neglected in the present work, as proposed in Ref. [9]. The pressure correction field obtained through the resolution of the previous equations is used to correct three velocity components in each control volume face, using expressions like the one presented next for the west

face:

$$u_{\mathrm{W}} = u_{\mathrm{W}}^* + \left[\frac{1}{a_{\mathrm{P}}^u - \sum a_{\mathrm{nb}}} \left(J\xi_x \frac{\partial P'}{\partial \xi} + J\eta_x \frac{\partial P'}{\partial \eta} + J\zeta_x \frac{\partial P'}{\partial \zeta} \right) \right]_{\mathrm{W}}$$

$$v_{\mathrm{W}} = v_{\mathrm{W}}^* + \left[\frac{1}{a_{\mathrm{P}}^v - \sum a_{\mathrm{nb}}} \left(J\xi_y \frac{\partial P'}{\partial \xi} + J\eta_y \frac{\partial P'}{\partial \eta} + J\zeta_y \frac{\partial P'}{\partial \zeta} \right) \right]_{\mathrm{W}} \qquad (16)$$

$$w_{\mathrm{W}} = w_{\mathrm{W}}^* + \left[\frac{1}{a_{\mathrm{P}}^w - \sum a_{\mathrm{nb}}} \left(J\xi_z \frac{\partial P'}{\partial \xi} + J\eta_z \frac{\partial P'}{\partial \eta} + J\zeta_z \frac{\partial P'}{\partial \zeta} \right) \right]_{\mathrm{W}}$$

where

$$\frac{\partial P'}{\partial \xi} = P'_{(i,j,k)} - P'_{(i-1,j,k)}$$

$$\frac{\partial P'}{\partial \eta} = \frac{P'_{(i-1,j+1,k)} + P'_{(i,j+1,k)} - P'_{(i-1,j-1,k)} - P'_{(i,j-1,k)}}{4}$$

$$\frac{\partial P'}{\partial \zeta} = \frac{P'_{(i-1,j,k+1)} + P'_{(i,j,k+1)} - P'_{(i-1,j,k-1)} - P'_{(i,j,k-1)}}{4}$$

The discretized transport equations are solved using the tridiagonal matrix algorithm (TDMA) [7] with sweeps in the three computational directions. For the pressure correction equation, a three-level multigrid technique [10] is used in conjunction with the TDMA.

Boundary Conditions

Due to the symmetry of the problem, the computations were carried out in half of the physical domain. Velocity, temperature, and turbulence quantities are specified at the inlet of the domain. These were obtained as a solution of the respective transport equations when the gradients in the two directions perpendicular to the flow vanish, a situation that corresponds to a developed flow over a flat plate, with an imposed boundary layer height. At the other boundaries, except for the ground, the second derivatives of scalars are made equal to zero. At the bottom boundary (the ground), an adiabatic condition is imposed for the energy equation, while for momentum, a no-slip impervious boundary is considered. The contravariant velocity components perpendicular to the boundaries are constrained by global mass conservation.

Due to the nature of the staggered grid, the boundary conditions for scalars and for the Cartesian velocity components parallel to the boundaries are imposed by recourse to fictitious points lying outside the computational domain.

The main steps of the numerical procedure can be summarized as follows.

1. Initialization of the variables.
2. Imposition of boundary conditions through computation of the variables of the fictitious points.
3. Computation of the coefficients for the momentum and P' equations.

4. Resolution of one momentum equation per control volume.
5. Computation of the contravariant velocities.
6. Imposition of global mass conservation by assigning proper values to the contravariant velocities at the boundaries.
7. Computation of the source term for the P' equations.
8. Calculation of the P' field.
9. Correction of the three Cartesian velocities in each face of the control volumes, and calculation of the new contravariant velocities.
10. Correction of the pressure field.
11. Calculation of the coefficients of the transport equations for other scalars (T, k, and ε).
12. Resolution of the transport equations for other scalars.
13. Return to step 2, until prespecified convergence criteria are satisfied.

The algorithm previously described proved to be very stable and robust, with excellent capabilities to predict a wide range of flows. Memory storage requirements are higher than for a Cartesian approach, due to the necessity of storage of two additional velocity components in each control volume face, as well as the metric relations. Computer time, however, is not significantly higher than that typically needed for Cartesian calculations.

THE FIRE SPREAD MODEL

The model for fire propagation used in the present study can be decomposed in three main parts:

- Fire rate of spread in the direction of maximum spread is computed using the equations proposed by Rothermel [1].
- A model of double ellipse is used to compute fire spread in any arbitrary direction [11].
- The fire propagation from cell to cell is computed using Dijkstra's dynamic programming algorithm [12].

Each of these parts will be presented separately below.

Rothermel's Model for Fire Spread Calculation

Rothermel's model [1] is an empirical fire-spread model, developed essentially from laboratory experiments (as opposed to field experiments), using three artificial fuels (random excelsior fuel beds, regular-geometry fuel beds made of wood sticks arranged in two configurations, and grasslike natural fuel beds). The model was developed for a stationary fire spread in a statistically homogeneous fuel bed, at least in what concerns relevant parameters, and is not suited to be applied to high-intensity fires, crown fires, or fires where spotting plays a relevant role in fire spread. A recent review of Rothermel's model is presented in Ref. [13].

The keystone of the model is Eq. (17), which expresses an energy balance within a unit volume of the fuel ahead of the flame. It illustrates the concept that

the rate of spread $\mathbf{R}$ is just a ratio between the rate of heating of the fuel, and the energy required to bring that same fuel to ignition.

$$\mathbf{R} = \frac{I_r \pi (1 + \boldsymbol{\phi}_w + \boldsymbol{\phi}_s)}{\rho_b \omega Q_i} \tag{17}$$

where $\mathbf{R}$ is rate of spread (m/s), I_r is reaction intensity (heat released per unit area of the flame front) [J/(m² s)], π is the propagating flux ratio (fraction of heat release that is responsible for fuel heating and consequent ignition), $\boldsymbol{\phi}_w$ is the wind factor, $\boldsymbol{\phi}_s$ is the slope factor, ρ_b is bulk density (mass of fuel per unit volume) (kg/m³), ω is the effective heating number (ratio between the bulk density and the mass of fuel involved in the ignition process), and Q_i is the heat of pre-ignition (heat required to bring a unit weight of fuel to ignition) (J/kg).

All the quantities in Eq. (17) are calculated using the fuel and environmental characteristics supplied by the user, which are

- oven-dry fuel loading (kg/m²)
- fuel depth (m)
- fuel particle surface-area-to-volume ratio (m⁻¹)
- oven-dry particle density (kg/m³)
- fuel particle moisture content as a fraction of dry weight
- fuel particle mineral content
- wind speed and direction at midflame height (m/s)
- terrain topography (slope and direction of maximum slope)

A detailed explanation of this fire spread model and respective equations is given in Ref. [1].

The effect of wind and slope is described by the two coefficients $\boldsymbol{\phi}_w$ and $\boldsymbol{\phi}_s$ in Eq. (17). The quantity $\mathbf{1}$ is a unity vector aligned with the vector $\boldsymbol{\phi}_w + \boldsymbol{\phi}_s$, which takes into account the isotropic component of the fire rate of spread for a situation of no wind and no slope.

The Double Ellipse Model

Rothermel's model gives as output the spread rate in the maximum spread direction, but it does not provide any information about fire size and shape. Information concerning these two parameters is, however, of vital importance for fire control and suppression. A forest fire burning in nonhorizontal terrain, or burning under windy atmospheric conditions, acquires an approximately elliptical shape. Anderson [11], using data from several fire experiments, proposed a two-semi-ellipse fire-shape model, whose equations, Eqs. (18), are used in the present study to compute the size and shape of a fire. The equations correspond to the diagram in Figure 3.

$$c = 0.492 e^{(-0.1845 V_{eq})} \qquad p = 0.542 e^{(-0.1483 V_{eq})}$$

$$a_1 = 2.502 (88 V_{eq})^{-0.3} \qquad a_2 = 1 + c - a_1 \tag{18}$$

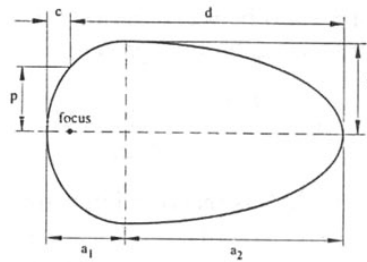$$b = 0.534 e^{(-0.1147 V_{eq})} \qquad d = 1$$

Figure 3. Anderson's [11] two-semi-ellipse fire-shape model. Parameters are defined by Eq. (18).

The ellipse parameters presented in Eq. (18) are nondimensionalized by the fire-spread distance measured in the direction of maximum spread. The variable V_{eq} in Eqs. (18) is an equivalent velocity that combines both the effects of velocity and slope on fire propagation, and it is defined as

$$V_{eq} = |\mathbf{V}_{eq}| \qquad \mathbf{V}_{eq} = \mathbf{V}_w + \mathbf{V}_s \tag{19}$$

where $\mathbf{V}_w$ is the wind velocity at midflame height and $\mathbf{V}_s$ a hypothetical wind velocity that would produce an effect equivalent to the one produced by local slope, on fire characteristics.

Dijkstra's Algorithm

In most forest fires, as may be expected, fuel characteristics have large spatial variations. Rothermel's model, however, was developed for homogeneous fuel beds. Therefore, simulation of fire growth in the presence of spatial nonhomogeneities of the various parameters governing fire spread requires a subdivision of the domain in cells, in which the input conditions are assumed as locally homogeneous. In the present case, the fuel is considered as homogeneous, and the spatially changing conditions are slope, wind velocity, and wind direction. Starting with a certain number of ignited cells, the fire-spread calculation is a matter of finding the next cell to ignite, which may not be the closest one. Dijkstra's dynamic programming algorithm is thus a procedure designed to find the shortest path between a specified pair of nodes. For each burning cell, the time that the fire takes to propagate to all its "neighbors" is computed with Rothermel's model and the two-semi-ellipse model. The instant of time for which each nonburning cell may be ignited is computed, and the next cell to ignite will be the one with the lowest assigned value.

The concept of "neighborhood" plays, in the present context, a particularly important role. For a given burning cell, the number and position of surrounding cells, defined as neighbors, have a decisive role in the accuracy of the simulated fire shape [14], relative to the correct solution taken as the ellipse. Figure 4 depicts a generic burning cell, represented by the shaded rectangle, and the corresponding neighbors considered in the present work.

THE OVERALL MODEL

Interaction between the fire-spread model and flow-field calculations is undertaken through a process of sequential computations, in which the velocity field obtained in a certain time instant is used as input to Rothermel's fire-spread model, and vice versa. This process is described in more detail in the subsequent sections.

Grids

For computational expediency, and within the objectives and expected accuracy of the model used in the present study, the calculations were carried out in two different grids; a coarse, three-dimensional grid, where temperature and velocity fields were computed; and a finer, quasi-two-dimensional grid, mapping the ridge surface, where fire size and shape were calculated. Information between these two grids is interchanged through linear three-dimensional interpolation.

Interaction of Fire and Flow Field

The heat released by the fire is responsible both for ignition of the fuel ahead of the flame front, due to heat transfer to the fuel, as well as for heating of the air and soil. Rothermel's model provides a means of quantifying both the total heat release and the part of this heat absorbed by the fuel, by defining the variable π, the propagating flux ratio. For the remaining energy, based on some experimental evidence, it was considered that 15% was absorbed by the soil and 85% was responsible for air heating. Treatment of the fuel bed immediately after the passage of the flame front was done by assigning an exponential decay of heat release, using a physically realistic relaxation time chosen to match field data.

Effects of fire on the velocity and temperature fields were introduced in the numerical model by imposing a volumetric heat release through the first row of control volumes adjacent to the surface. The amount of heat release was computed as a linear function of the burning ground area.

Numerical Procedure

The solution is carried out iteratively, starting with a nearly punctual fire. Taking as initial condition the velocity field computed for an isothermal situation, a few newly ignited cells are computed in the "fine grid," and the instant of time at
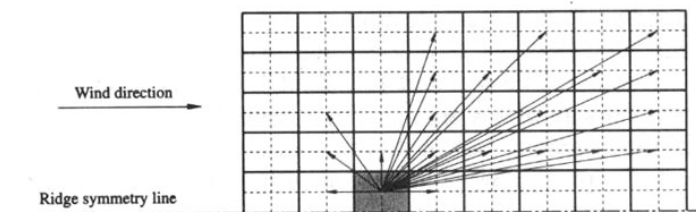

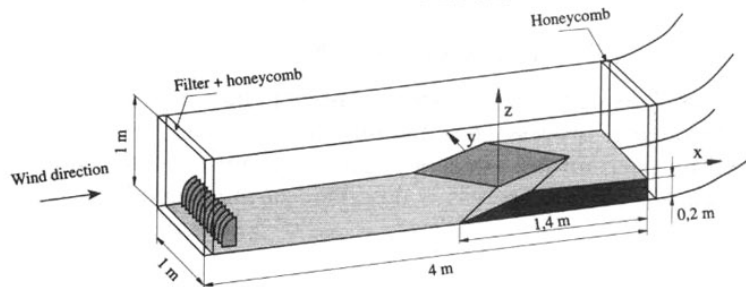**Figure 4.** Definition of "neighborhood" considered in the present work.

Figure 5. Schematic view of the wind tunnel.

which each cell ignites is registered. The computation is then transferred to the "coarse grid," where the heat release rate through each control volume is calculated as a linear function of the percentage burning area of the control volume. Velocity, temperature, and turbulent quantities are solved, and after convergence of the iterative method, the new velocity field is interpolated to the fine grid, and a few new cells are ignited. The process is continued until the burning/burned area reaches a specified limit.

The progression of the process with time is thus controlled by the combustion model. To avoid very large changes in the velocity field, the number of cells ignited within each cycle is made sufficiently small, typically around 10% of the already ignited cells.

VALIDATION OF THE NUMERICAL MODEL

The numerical model for turbulent flow calculations presented here was validated against experimental results obtained in a wind tunnel. The wind tunnel used in the experiments had a closed test section of 1×1 m and was of the suction type. Due to the relatively short distance available to uniformize the flow and develop a turbulent boundary layer, a set of 12 shark teeth was positioned at the inlet section, along with a honeycomb and a filter, as shown in the schematic view of the wind tunnel represented in Figure 5.

The wind tunnel experiments were not designed to simulate the actual conditions. Instead, the aim was the validation of the numerical model for the calculation of turbulent flow. Thus, for experimental convenience, the geometry shown in Figure 1 was slightly modified through the introduction of a horizontal flat plate downstream of the point of intersection of the two slopes and the ground. The ridge shape used in the experimental setup can be seen in Figure 6, which also represents the grid used in the numerical calculations. The values for the angles α and θ corresponding to this configuration are 90° and 30°, respectively.

The comparison between numerical and experimental results was made for an isothermal situation. The incident turbulent boundary layer was characterized by a free stream velocity of 4.4 m/s and by a boundary layer height of 0.16 m. In order to check the symmetry of the flow and to establish the effects of the lateral wall, several velocity profiles were measured with a Pitot tube, in the region of the ridge, at different distances from the vertical plane of symmetry. Results indicate that the flow is quite symmetric, exhibiting nevertheless a marked wall effect in the regions where $y > 0.2$ m or $y < -0.2$ m. Some of the experimental velocity

profiles obtained are represented in Figure 7a where the velocity is nondimensionalized by the free stream velocity. Figure 7b depicts the experimental velocity profile obtained at the wind tunnel symmetry plane, along with the incident velocity profile obtained from the numerical simulations.

The comparison of the experimental and numerical results is presented here in terms of the distribution of the pressure coefficient c_p, defined in Eq. (20), along the x direction:

$$c_p = \frac{P_w - P_0}{0.5 \rho U_0^2} \qquad (20)$$

For the measurement of c_p, a total of 230 pressure taps were made on the surface of the model, in its right side ($y < 0$). Figure 8 shows some of the measurements obtained, for various distances to the ridge symmetry plane. In these figures the slope region is represented by the thick line in the lower part of the graphics. Analysis of these graphics shows very good agreement between the experimentally and numerically obtained values. The initial increase of c_p, due to a partially stagnant region near the slope, is followed by an abrupt drop of pressure motivated by the accelerating flow. Values of c_p reach a minimum slightly after the transition to the downstream horizontal plate. This minimum was not fully predicted by numerical simulation, particularly in the regions far away from the ridge symmetry plane. This slight discrepancy is probably caused by the boundary layer characteristics prevailing in these regions, as indicated in Figure 7a. Possible limitations of the turbulence model may also have largely contributed to this discrepancy.

ISOTHERMAL FLOW OVER THE RIDGE

Before presenting the fire propagation results, it is helpful to understand how the isothermal flow field depends on the ridge geometry. For this purpose, several
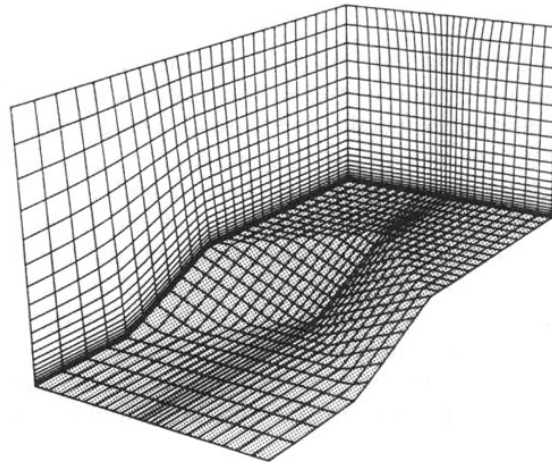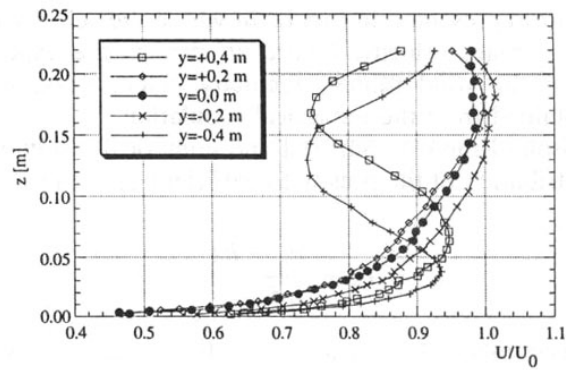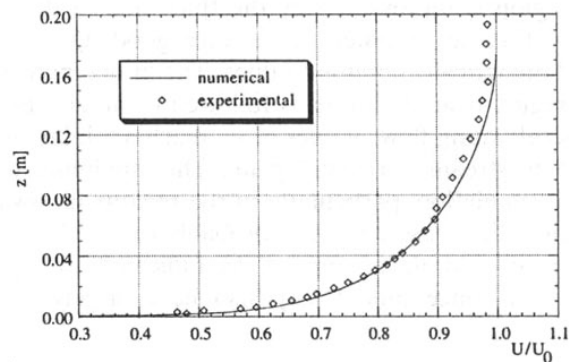

**Figure 6.** Grid used for the numerical experiments concerning the validation of the algorithm.

Figure 7. Boundary layer profile. (*a*) Experimental values for different distances from the wind tunnel plane of symmetry. (*b*) Comparison between numerical and experimental values at the wind tunnel symmetry plane.

different ridge configurations were considered, with each geometry defined by a fixed combination of the angles α and θ, the angle of intersection of the slopes and the angle of inclination, respectively (Figure 1). The geometries studied may be grouped into two different sets. In the first set, S_1, the angle θ was kept constant, while α was changed. In the second set, S_2, both α and θ were changed in such a way that the angle ψ, the angle of inclination of the slopes in the main flow direction, remained constant. Computations were carried out for each geometry listed in Table 1, and the free stream velocity was taken as 7 m/s. After some grid independence tests, a grid with $22 \times 14 \times 22$ nodes in the x, y, and z directions, was chosen to carry out the computations.

Unlike the situation simulated in the wind tunnel, all the boundaries were considered as pervious to the flow, except for the bottom boundary, which corresponds to the ridge.

The characteristics of the flow field for the isothermal situation were investigated for the different geometries in terms of the variation of the magnitude of the

velocity as a function of the coordinate x, at a constant height above the ground, at the ridge symmetry plane. The results presented in Figure 9a correspond to S_1, for a constant height of 3 m above the ground. Keeping in mind that the different situations correspond, in this case, to a change in the angle α, examination of the figure reveals that an increase of this angle has the effect of decreasing the flow velocity near the region of intersection of the slopes, due to a localized blockage
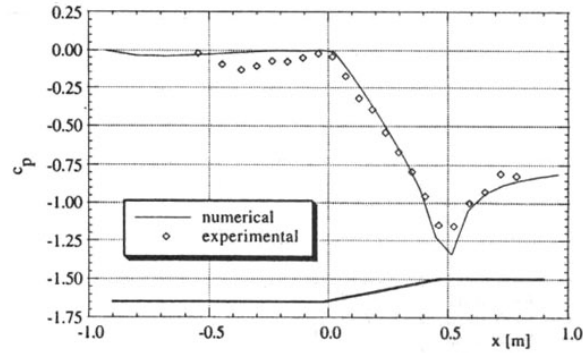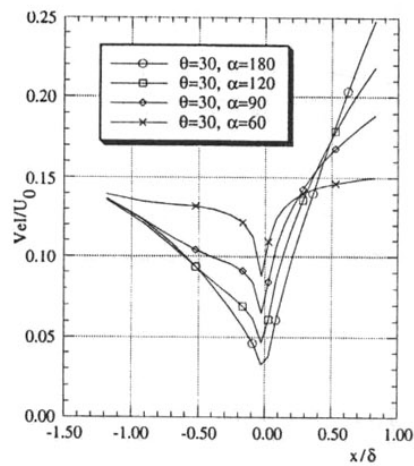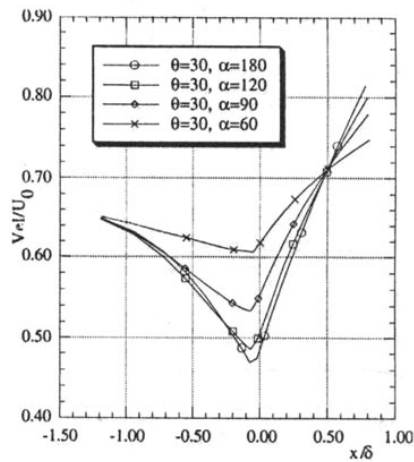
(a)
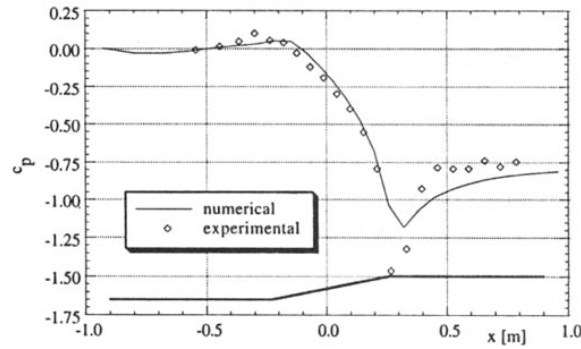
(b)
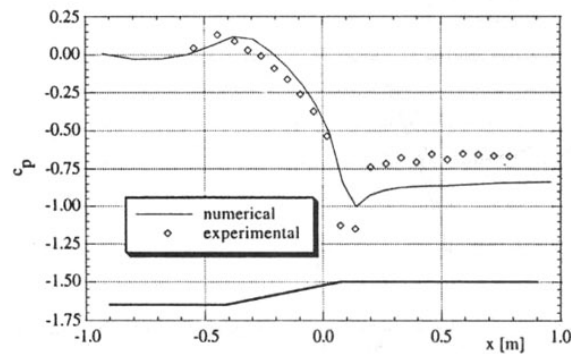
(c)

Figure 8. Experimental versus numerical distribution of c_p: (a) $y = -1.8$ cm, (b) $y = -23$ cm, (c) $y = -41$ cm.

Table 1. Angles Characterizing the Geometries Considered

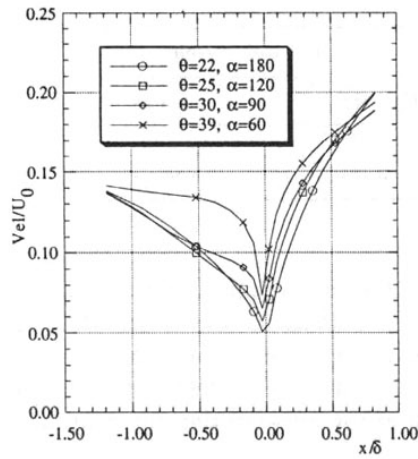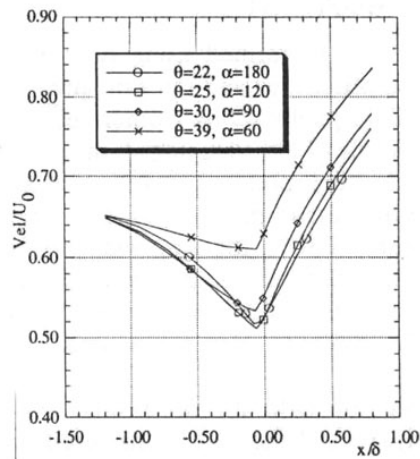|	Set 1			Set 2	
θ	α	ψ	θ	α	ψ
30	60	16.10	39.23	60	22.21
30	90	22.21	30	90	22.21
30	120	26.57	25.24	120	22.21
30	180	30	22.21	180	22.21

(a)

(b)

Figure 9. Velocity magnitude at a constant height above the ground, in the symmetry plane for set S_1: (a) height 3 m, (b) height 30 m.

(a)

Figure 10. Velocity magnitude at a constant height above the ground, in the symmetry plane for set S_2: (a) height 3 m, (b) height 30 m.

(b)

effect. Taking into account that an increase of α corresponds, in S_1, to an increase of the slope angle in the main flow direction, one can understand the acceleration occurring at the outlet of the domain, which becomes more accentuated for higher values of α. For comparison purposes, the results for a height of 30 m above the ground are shown in Figure 9b.

The numerical experiments indicate that a decrease of α produces increased flow velocities near the slope intersection region, which is physically plausible. In these experiments, the angle ψ was not kept constant. However, it might be of interest to fix this value to aid in further understanding of the flow. Configurations S_2 contemplate a constant value ψ by varying accordingly α and θ, which will be called a change in the ridge effect. These results are presented in Figures 10a and 10b for heights of 3 m and 30 m above the ridge surface, respectively.

Table 2. Characteristics of the Fuels

	Reaction intensity, kW/m^2	Rate of spread, m/min	
		$U_0 = 0$ m/s	$U_0 = 5$ m/s
Fuel a	501	1.2	66
Fuel b	465	0.174	3.54

Examination of these graphs shows that the single point of intersection of the curves tends to disappear. This implies that an increase of the ridge effect results in an overall enhancement of the flow velocity, a fact that was not verified in set S_1. As a conclusion, we may say that a change in the angle of intersection of the slopes plays as important a role in flow acceleration as the angle of the slopes in the main flow direction.

RESULTS FOR FIRE PROPAGATION

Numerical simulations of fire growth were performed using two different types of fuel, characterized by distinct reaction intensities and rates of spread. The characteristics of the fuels were taken from data published by Rothermel [1], and they correspond to a tall grass field and to debris of light logging slash, hereafter designated as fuel models a and b, respectively (fuel models 2 and 9, respectively, in Ref. [1]). As a reference, the characteristic fire-spread rate and reaction intensity for these two fuels, considering a fuel moisture of 10%, for a no-wind condition, and for an incident wind speed of 5 m/s, both in flat terrain, are given in Table 2. It can be seen from this table that these two fuels are characterized by quite different typical rates of spread, as well as by different relative reactions to wind speed.

The grids used for the calculation of air flow field and fire propagation are depicted in Figures 11a and 11b, respectively. For all the cases considered, which correspond to the ridge configurations listed in Table 1, the fire was ignited at the point of intersection of the slopes with the ground, and the incident wind velocity was set to 7 m/s. Figure 12a represents the fire growth, for fuel a, in terms of burning and burned areas as a function of the time elapsed since fire start, for S_1. Figure 12b depicts the same result for S_2. These graphs clearly indicate an initial fire acceleration phase, followed by a transition to a steady state regime. The dependence of fire-spread velocity with the geometry of the ridge is in accordance with the velocity field characteristics examined in the previous section. Also apparent from these plots is that the differences in fire rate of spread for the several geometric ridge configurations are more pronounced at the initial stages of fire growth. The fire shape for fuel a, for three different ridge configurations, may be observed in Figure 13, where the shaded areas are the fire contours at the specified times. The time origin is the instant of fire ignition ($t = 0$), and in these figures the velocity vectors correspond to the latest instant of time. The difference in plume shape for these two situations is clearly noticeable. Figure 14 shows the corresponding results for fuel b.

An interesting feature arising from the comparison of fire shapes is the different response of the two fuels to the interaction of wind and slope. This feature is evident if one examines the fire shapes corresponding to each of the fuels, for the geometries ($\theta = 39°$, $\alpha = 60°$) and ($\theta = 30°$, $\alpha = 90°$). Fuel b, with its lower sensitivity to wind effects, tends to spread in a direction closer to the main slope direction, with a consequent formation of two independent symmetrical fronts. As a final look at the global features of the fire propagation for the different geometries and both fuels, Table 3 presents the percentage increment of time necessary for the fire to reach an area of 5000 m^2, when the geometry of the ridge is changed between the two extreme configurations in each set, i.e., from ($\theta = 30°$, $\alpha = 60°$) to ($\theta = 30°$, $\alpha = 180°$) in S_1 and from ($\theta = 39°$, $\alpha = 60°$) to
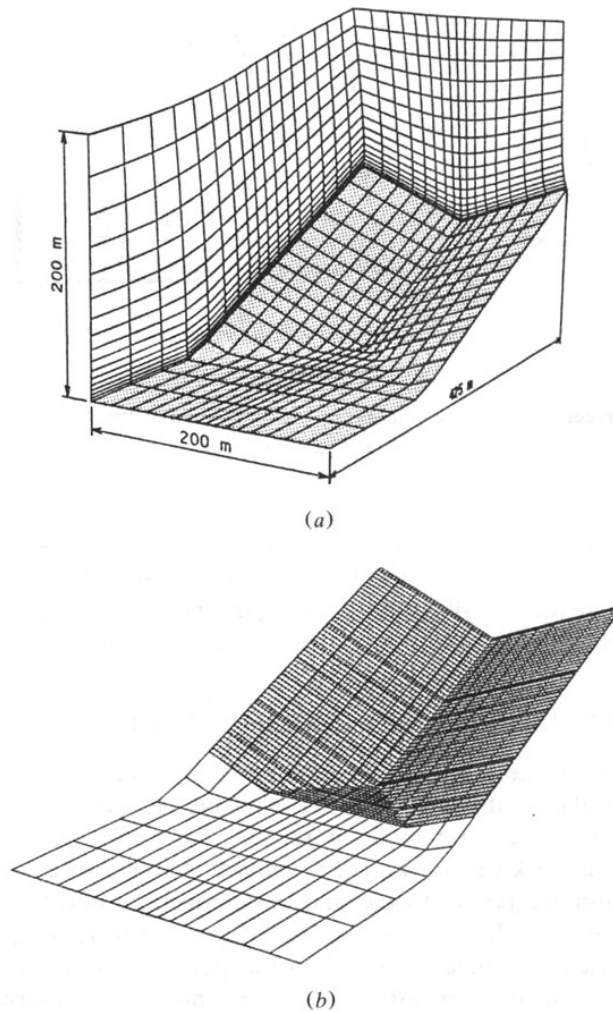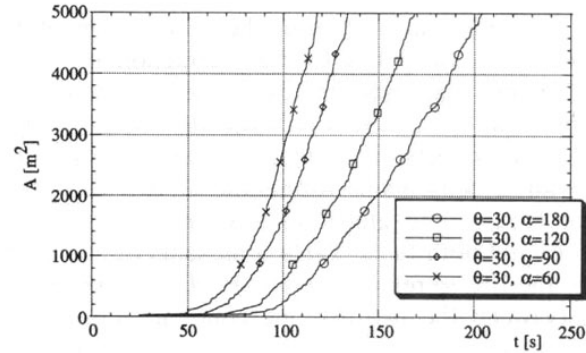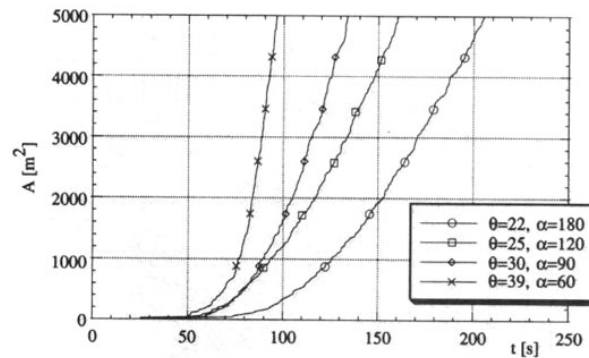

(a)

(b)

Figure 11. Grids used for the case ($\theta = 30°$, $\alpha = 90°$): (a) coarse grid for air flow calculation, (b) fine grid for fire-shape calculation.

(a)

(b)

Figure 12. Burning and burned area (A) as a function of time,
(a) configurations S_1, (b) configurations S_2.

($\theta = 22°$, $\alpha = 180°$) in S_2. The results listed in this table clearly show that the fire-spread velocity for the lighter fuel, fuel a, is more sensitive to the ridge configuration than fuel b, with both fuels experiencing a marked increase of fire spread with "tighter" ridges, with more pronounced effects for S_2.

DISCUSSION AND CONCLUDING REMARKS

Fire behavior is the result of complex, interrelated phenomena, and even with the best present-day mathematical tools available, it cannot be described and predicted in quantitative terms with more than fair accuracy. Consequently, the aim of the present work was to predict the major characteristics of fire spread, as seen from a qualitative point of view, and to demonstrate how the ridge geometry can significantly modify fire behavior as related to other terrain topographies, with consequent increase in danger and risk to the personnel directly involved in the fire. The results for fire spread and growth show the remarkable role that topography has on fire spread, stressing the fact that, although the terrain slope is a relevant factor, the overall geometry may be even more important. In the present

case, the ridge proved to have an important role in flow acceleration, with evident consequences in the fire rate of spread. This effect is more pronounced for fuels with a characteristic rate of spread more sensitive to wind speed, such as light fuels. One must be aware that the procedure for the calculation of rate of fire spread presented here is just a first approximation. Nevertheless, it takes into account in a realistic way the dynamic interaction between fire spread and consequent changing conditions in the case of complex geometries. It is by far superior to a stationary approach, and it may prove to be a useful tool to study the behavior of open, large-scale fires.
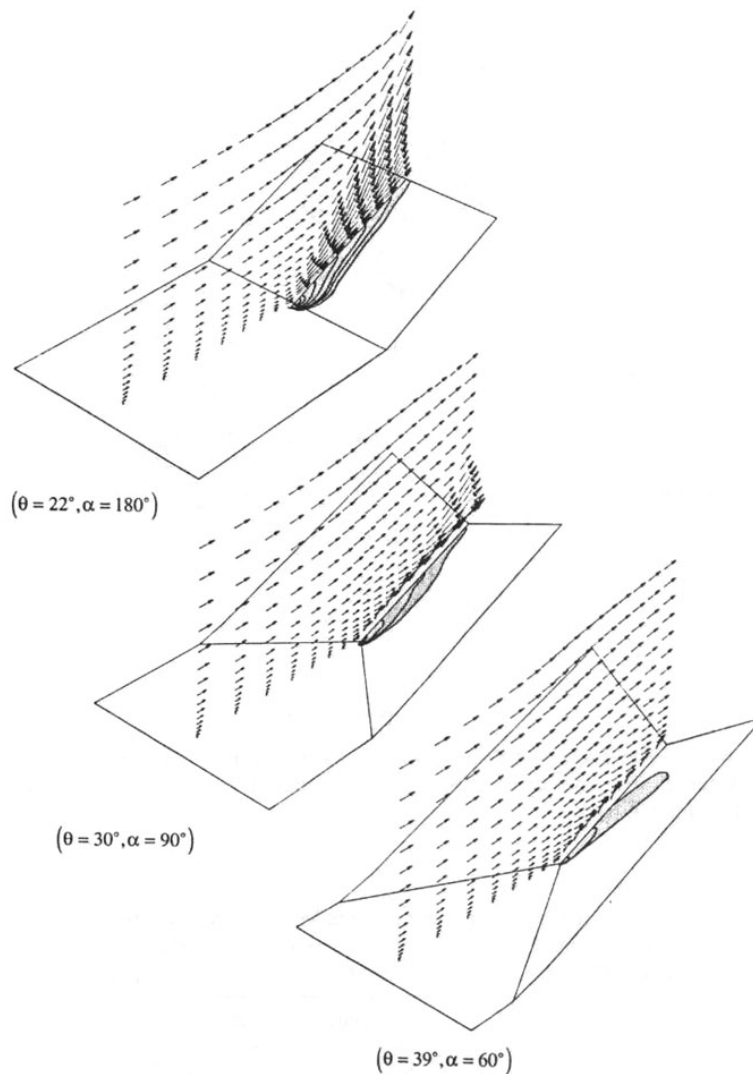

Figure 13. Fire-shape and velocity vectors for incident free stream velocity of 7 m/s, fuel a, first contour for time 50 s, time interval between contours 25 s, and configurations S_2.

$\left(\theta = 22°, \alpha = 180°\right)$

$\left(\theta = 30°, \alpha = 90°\right)$
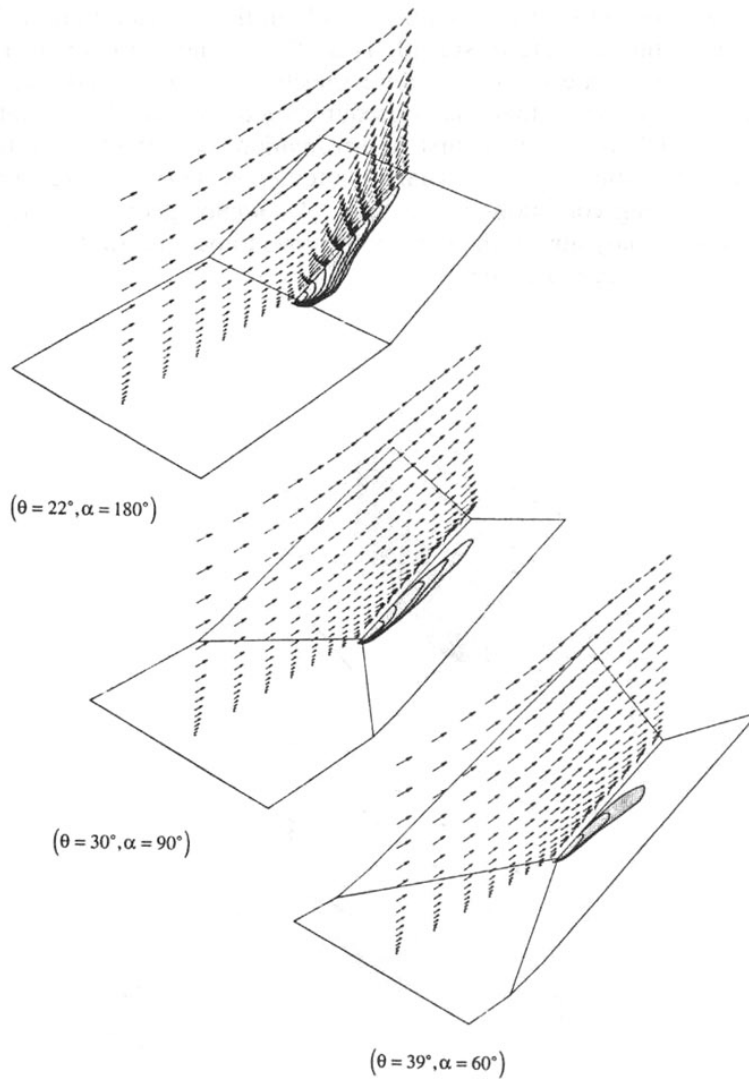
$\left(\theta = 39°, \alpha = 60°\right)$

Figure 14. Fire-shape and velocity vectors for incident free stream velocity 7 m/s, fuel b, first contour for time 1000 s, time interval between contours 250 s, and configurations S_2.

Table 3. Percentage Increment of Time Necessary for the Fire to Reach an Area of 5000 m² , when the Geometry of the Ridge is Changed Between the Two Extreme Configurations in Each Set

	Time increment, %	
	Set 1	Set 2
Fuel a	73	114
Fuel b	58	82

REFERENCES

1. R. C. Rothermel, A Mathematical Model for Predicting Fire Spread in Wildland Fuels, USDA F.S. Research Paper INT-115, 1972.
2. R. C. Rothermel, How to Predict the Spread and Intensity of Forest and Range Fires, General Technical Report INT-143, USDA, Ogden, Utah, 1983.
3. J. F. Thompson, F. C. Thames, and C. W. Mastin, Automatic Numerical Generation of Body-Fitted Curvilinear Coordinate System for Field Containing Any Number of Arbitrary Two-Dimensional Bodies, *J. Comput. Phys.*, vol. 15, pp. 299–319, 1974.
4. C. Zhang and A. C. M. Sousa, Numerical Simulation of Turbulent Shear Flow in an Isothermal Heat Exchanger Model, *J. Fluids Eng.*, vol. 112, pp. 48–55, 1990.
5. D. A. Anderson, *Computational Fluid Mechanics and Heat Transfer*, Hemisphere, New York, 1985.
6. F. H. Harlow and J. E. Welch, Numerical Calculation of Time Dependent Viscous Incompressible Flow with a Free Surface, *Phys. Fluids*, vol. 8, pp. 2182–2189, 1965.
7. S. V. Patankar, *Numerical Heat Transfer and Fluid Flow*, Hemisphere, Washington, D.C., 1980.
8. J. P. Van Doormaal and G. D. Raithby, Enhancements of the Simple Method for Predicting Incompressible Fluid Flows, *Numer. Heat Transfer*, vol. 7, pp. 147–163, 1984.
9. W. Shyy, S. S. Tong, and S. M. Correa, Numerical Recirculating Flow Calculation Using a Body-Fitted Coordinate System, *Numer. Heat Transfer*, vol. 8, pp. 99–113, 1985.
10. M. E. Braaten and W. Shyy, Study of Pressure Correction Methods with Multigrid for Viscous Flow Calculation in Non-Orthogonal Curvilinear Coordinates, *Numer. Heat Transfer*, vol. 11, pp. 417–442, 1987.
11. E. A. Anderson, Predicting Wind-Driven Wildland Fire Size and Shape, USDA F.S. Research Paper INT-305, 1983.
12. E. W. Dijkstra, A Note on Two Problems in Connection with Graphs, *Numer. Math.*, vol. 1, pp. 269–271, 1959.
13. C. S. A. André, A. M. G. Lopes, and D. X. Viegas, A Broad Synthesis of Research on Physical Aspects of Forest Fires, Cad. Cient. Inc. Forestais, no. 3, Coimbra, 1992.
14. U. Feunekes, Error Analysis in Fire Simulation Models, M.Sc. thesis, Department of Forest Research, University of New Brunswick, Canada, 1991.